


Cite this: *Nanoscale*, 2023, **15**, 2932

# Preclinical safety assessment of red emissive gold nanocluster conjugated crumpled MXene nanosheets: a dynamic duo for image-guided photothermal therapy†

Barkha Singh,<sup>a,b</sup> Rohan Bahadur,<sup>b</sup> Priyanka Maske,<sup>b</sup> Mayuri Gandhi,<sup>a</sup> Dipty Singh<sup>\*c</sup> and Rohit Srivastava <sup>\*b</sup>

Red emissive gold nanoclusters have potential as biological fluorescent probes, but lack sufficient light-to-heat conversion efficiency for photothermal therapy (PTT). MXene nanomaterials, on the other hand, have shown promise in PTT due to their strong near-infrared absorption abilities, but their instability caused by restacking of the sheets can decrease their available surface area. One approach to address this issue is to design sheets with wrinkles or folds. However, the crumpled or 3D MXene materials reported in the literature are actually aggregates of multiple nanosheets rather than a single sheet that is folded. In this study, a modified method for crumpling a single MXene sheet and further conjugating it with red emissive gold nanoclusters and folic acid was developed. A detailed *in vitro* toxicity study was performed in various cell lines and cellular uptake in cancer cells was studied using AFM to understand its interaction at the nano–bio interface. The material also demonstrated excellent utility as a bioimaging and PTT agent *in vitro*, with its high fluorescence allowing bioimaging at a lower concentration of 12  $\mu\text{g mL}^{-1}$  and a photothermal conversion efficiency of 43.51%. *In vitro* analyses of the cell death mechanisms induced by PTT were conducted through studies of apoptosis, cell proliferation, and ROS production. *In vivo* acute toxicity tests were conducted on male and female Wistar rats through oral and intravenous administration (20  $\text{mg kg}^{-1}$  dose), and toxicity was evaluated using various measures including body weight, hematology, serum biochemistry, and H&E staining. The findings from these studies suggest that the MXene gold nanoconjugate could be useful in a range of biomedical applications, with no observed toxicity following either oral or intravenous administration.

Received 17th October 2022,  
Accepted 2nd January 2023

DOI: 10.1039/d2nr05773e

rsc.li/nanoscale

## 1. Introduction

The alarming rate of increase in cancer mortality has driven extensive research in the field of oncology, leading to the development of numerous cancer treatments. Surgical excision, chemotherapy, and radiation therapy are at the forefront of anticancer treatment; however, the adverse effects of these treatments are widely documented. Cancer theranostics rep-

resents a combination of therapeutics and diagnostics. The primary goal of cancer nanotheranostics is to design a nano-composite consisting of both modalities, *i.e.*, diagnostic/imaging and therapy with enhanced specific cell targeting.<sup>1,2</sup> Nanoscale size-dependent features provide nanomaterials with unique specifications that are resilient in various medical applications.<sup>3–7</sup> Photothermal therapy (PTT) is a minimally invasive photo-based treatment that utilizes a photosensitizer, which can absorb electromagnetic radiation such as radiofrequency, microwaves, near-infrared irradiation, or visible light and convert it into heat. The resultant rise in tissue temperature causes hyperthermia, inducing programmed cell death.<sup>8</sup> Selective delivery and the use of an imaging instrument for visualizing and analyzing the distribution of photoactive agents in tumors and other organs are required to achieve the intended PTT effects with fewer adverse effects. As a result, developing a targeted theranostic system that combines PTT and imaging capabilities is key to developing an advanced nanomaterial.

<sup>a</sup>Centre for Research in Nano Technology & Science (CRNTS), Sophisticated Analytical Instrument Facility (SAIF), IIT Bombay, Powai, Mumbai, 400076, India. E-mail: 93barkhasingh@gmail.com, mngandhi@iitb.ac.in

<sup>b</sup>Department of Biosciences and Bioengineering, Indian Institute of Technology (IIT) Bombay, Powai, Mumbai, 400076, India. E-mail: rohanbahadur@gmail.com, priyamaske1104@gmail.com, rsvivasta@iitb.ac.in; Tel: +91 222 576 7746

<sup>c</sup>Department of Neuroendocrinology, National Institute for Research in Reproductive and Child Health (NIRRH), Parel, Mumbai, 400012, India.

E-mail: singhd@nirrh.res.in

† Electronic supplementary information (ESI) available. See DOI: <https://doi.org/10.1039/d2nr05773e>

Noble metal nanoclusters (NCs), because of their ultrafine size and lack of toxicity, are more attractive for biolabeling and bioimaging applications than semiconductor quantum dots (QDs) which generally contain hazardous metal species *e.g.*, cadmium and lead.<sup>9,10</sup> Gold nanoclusters (Au NCs) are incredibly versatile and have been explored as bioimaging probes for image-guided therapy because of their ultrafine size, unique molecule-like properties, photostability, large Stokes shift, long luminescence lifetime, and nontoxicity.<sup>11–14</sup> Satisfactory biodistribution and renal clearance are other features that could pave the way for enhanced *in vivo* treatment outcomes.<sup>15–17</sup> Au NCs can be energetically considered as molecules when significant quantization of the conduction band occurs due to the quantum confinement phenomenon resulting in distinct optical features such as fluorescence upon light activation.<sup>18</sup> Possession of strong red/NIR luminescence properties makes Au NCs highly suitable fluorescent nanomaterials for bioimaging. Despite these advantages, Au NCs have significantly less phototherapeutic potential than typical photothermal agents such as gold nanorods or graphene oxide.<sup>19</sup> Owing to their easy chemical functionalization, Au NCs can be conjugated with a photosensitizer for light-mediated tumor ablation with bio-imaging.<sup>20</sup>

Large absorption cross-sections for optical wavelengths, minimal toxicity, ease of surface modifications, and high solubility in biocompatible solutions are all desirable characteristics for a photosensitizing agent.<sup>21</sup> 2D layered materials, such as chalcogenides, metal oxides, nitrides, sulphides, and carbides, have attracted a lot of attention as a result of progress in graphene research since its discovery.<sup>22,23</sup> MXenes are a group of two-dimensional (2D) transition-metal carbides and nitrides synthesized from the MAX phase where M is a transition metal (Ti, Ta, Nb, V, and Mo), A represents a group 13 or 14 element (Al, Si, Ge, Sn, S, As, P, In, Ga, Tl, and Pb) and X is C or N. The general chemical formula of MXenes is  $M_{n+1}X_nT_x$  ( $n = 1, 2, 3$ ) where  $T_x$  represents surface termination groups such as  $-OH$ ,  $=O$ , and  $-F$ .<sup>24–26</sup> MXenes have shown considerable promise in a variety of fields, including energy, batteries, supercapacitors, photocatalysis, and environmental remediation.<sup>27–30</sup> Owing to their low cytotoxicity, unique optical properties, and easy bulk synthesis, MXene nanosheets are also gaining popularity in biological applications,<sup>31</sup> particularly in regenerative medicine, antibacterial and anticancer therapies, and bio-imaging, although they are still in early stages.<sup>32,33</sup> The prominent challenges faced by pristine MXene nanosheets are oxidation, reduced surface area, and instability caused by their undesired self-restacking and aggregation. One of the ways to overcome this challenge is through electrostatically induced crumpling of MXene sheets to generate a 3D MXene structure.<sup>34–37</sup> This transformation from two dimensions to three dimensions can also improve surface functionalization and distribute properties evenly within the structure.<sup>38</sup> One of the easiest methods for producing a 3D MXene structure is alkali-induced crumpling.<sup>39</sup> However, the process causes the flocculation of numerous sheets to form a

3D architecture. The method can be modified to produce folds in single sheets instead of flocculation.

Prior to the therapeutic use of nanoparticles, it is essential to investigate the toxicity of the synthesized nanocomposite since the toxicity of a substance is strongly reliant on its composition, dose, length of treatment, and mode of administration (intravenous, intra-peritoneal, oral pulmonary, and intravitreal administration).<sup>40</sup> The most prevalent method of administering nanomaterials for PTT is the intravenous route; however, human exposure to nanomaterials may also occur orally. Consequently, it is necessary to test the toxicity of any nanomaterial using several administration routes before classifying it as non-toxic. Currently, the most common method for studying the *in vivo* toxicity of MXene-based formulations is intravenous injection. There is a significant gap in the current data on toxicity assessments of MXenes, particularly in terms of other modes of administration and assessments based on sex and reproductive organs.

MXenes coupled with other nanoparticles (Au, Ag, and Pd) were also created for various biomedical applications (Table S1†).<sup>41,42</sup> However, the use of MXenes in conjunction with gold nanoclusters in multimodal imaging-guided cancer therapy has seldom been documented. This work presents an improved method for crumpling MXene sheets simultaneously using heating and alkali treatment. The synthesized crumpled MXene nanosheets were further combined with gold nanoclusters to design a nanocomposite for the intended application in image-guided photothermal therapy. The study also evaluated the preliminary *in vivo* acute toxicity of the nanocomposite when administered orally and intravenously in Wistar male and female rats. Detailed acute toxicity analysis including body weight, organ weight, hematology, serum biochemistry and histopathology was performed to understand the administration mode-dependent toxicity/safety of this MXene based nanocomposite. The interaction and internalization of the material in breast cancer cells was examined using atomic force microscopy (AFM), while bioimaging was evaluated using confocal microscopy. In addition, a systematic *in vitro* photothermal therapy study was conducted, including analyses of cell death mechanisms through apoptosis, cell proliferation, and ROS production.

## 2. Experimental section

### 2.1 Material

**2.1.1 Synthesis chemicals.** The following chemicals were used for synthesis: titanium aluminum carbide powder ( $Ti_3AlC_2$ , MAX phase), hydrofluoric acid [HF (50% v/v)], tetramethylammonium hydroxide (TMAOH), sodium hydroxide (NaOH), chloroauric acid salt (Loba Chemie), triethylamine (TEA), 1-ethyl-3-(3-dimethylaminopropyl)carbodiimide hydrochloride (EDC), *N*-hydroxysuccinimide (NHS), folic acid (FA), dialysis membranes (Hi-Media), hydrochloric acid (HCl), and nitric acid ( $HNO_3$ ). All chemicals, unless stated, were procured from Sigma Merck.

**2.1.2 Cell culture experiments.** For cell culture experiments, Dulbecco's modified Eagle's medium (DMEM), fetal bovine serum (FBS), 1× phosphate buffered saline (PBS), antibiotic antimycotic solution 100× liquid (w/10 000 U penicillin, 10 mg streptomycin and 25 µg amphotericin B), and 1× trypsin-EDTA solution were procured from Hi-Media. Resazurin sodium salt, propidium iodide, 4',6-diamidino-2-phenylindole (DAPI), dichlorodihydrofluorescein diacetate (DCFDA), and phorbol 12-myristate 13-acetate (PMA) were procured from Sigma. An FITC Annexin V Apoptosis Detection Kit was procured from BD Biosciences.

## 2.2 Methodology

**2.2.1 Synthesis of gold nanoclusters (Au NCs) using egg albumin.** Egg albumin (white part of egg) was separated from the egg yolk. 1 part of egg albumin was diluted four times with Milli-Q water. 1 ml chloroauric acid salt (10 mM) was added to egg albumin at room temperature while stirring. After properly mixing, for 10 minutes, ~1 mL of 0.1 M NaOH was added (pH ~ 12). The solution was heated using microwave for 5–7 minutes until the color of the solution changed from light yellow to brown. The solution was kept overnight in the dark to grow and stabilize. The obtained solution was then dialyzed for purification and freeze dried for 48 hours. The Au NCs were obtained as a brown powder of gold nanoclusters which were further used in the study.

**2.2.2 Synthesis of crumpled MXene (c-Ti<sub>3</sub>C<sub>2</sub>).** Titanium aluminium carbide (Ti<sub>3</sub>AlC<sub>2</sub>) was slowly added to 10 mL of 50 wt% hydrofluoric acid (HF) with a final concentration of 0.1 g mL<sup>-1</sup>. The reaction was stirred for 48 hours. After 48 hours, the solution was centrifuged at 15 000 rpm for 30 min. The pellet was washed multiple times until the pH of the supernatant became 6. The obtained pellet (HF-Ti<sub>3</sub>C<sub>2</sub>) was freeze dried to obtain a black powder. The powder was immersed in equal wt% TMAOH and a dispersion was formed in water for the delamination process. The reaction was first bath sonicated for 30 min and then kept on a stirrer overnight. The solution was dialyzed and further freeze dried (TMA<sup>+</sup>-Ti<sub>3</sub>C<sub>2</sub>). To induce alkali-based crumpling, the above powder at 2.5 mg mL<sup>-1</sup> was heated at 80 °C and 2 M NaOH was added and stirred overnight. The solution was dialyzed and freeze dried to obtain black powder (c-Ti<sub>3</sub>C<sub>2</sub>).

**2.2.3 Conjugation of gold nanoclusters to crumpled MXene (Au@c-Ti<sub>3</sub>C<sub>2</sub>).** Crumpled MXene (c-Ti<sub>3</sub>C<sub>2</sub>) solution at a concentration of 100 µg mL<sup>-1</sup> was dispersed in 20 mL of water and 30 µL of triethylamine (TEA) was added. The solution was stirred for 10 min and then mixed with 40 mL of 100 µg mL<sup>-1</sup> Au NCs. Stirring was continued overnight. The solution was centrifuged, dialyzed and freeze dried to obtain Au@c-Ti<sub>3</sub>C<sub>2</sub> powder. In a separate experiment, gold nanoclusters were also conjugated on TMA<sup>+</sup>-Ti<sub>3</sub>C<sub>2</sub> to compare the effect of morphology on the loading percentage. The loading percentage was calculated using the ratio of gold and titanium evaluated using ICP-AES.

**2.2.4 Folic acid conjugation with the nanocomposite (FA-Au@c-Ti<sub>3</sub>C<sub>2</sub>).** First, the folic acid-NHS complex was syn-

thesized using the EDC-NHS coupling reaction. Briefly, 50 mg of folic acid was dissolved in 30 mL of dimethyl sulfoxide. 200 mg of EDC-HCl and 100 mg of NHS were added. The reaction was stirred overnight in the dark. The solution was filtered using a 0.2 µm syringe filter to remove unwanted by-products. Then, cold anhydrous diethyl ether containing 30% acetone was added to the solution to get a yellow precipitate. The solution was centrifuged at 15 000 rpm for 60 min at 10 °C. The resultant solution was lyophilized to get the NHS-folic acid complex. 20 µg of the FA-NHS was added to 1 mg mL<sup>-1</sup> solution of Au@c-Ti<sub>3</sub>C<sub>2</sub>. The resultant powder was dialyzed and freeze dried to obtain the final product FA-Au@c-Ti<sub>3</sub>C<sub>2</sub> which is a greenish black powder.

Characterization, *in vitro* experiments and *in vivo* methodology are provided in the ESI.†

**2.2.5 In vivo toxicity.** Animal experimentation was performed at the ICMR-National Institute for Research in Reproductive and Child Health (ICMR-NIRRH). The ethical permission for the same was obtained prior to conducting the experiment (IAEC no.: 12/21). Animal experimentation was performed in accordance with the guidelines of the Committee for the Purpose of Control and Supervision of Experimental Animals (CPCSEA), India.

## 3. Results and discussion

### 3.1 Synthesis of the gold MXene nanocomposite

The procedure for the synthesis of folic acid conjugated gold MXene composites is demonstrated in Scheme 1.

Amino acids, biomolecules, and polymers that act as functionalizing and reducing reagents are required for the preparation of stable and highly luminous Au NCs.<sup>43,44</sup> Herein, microwave assisted fluorescent Au NCs were synthesized using one-pot reduction of HAuCl<sub>4</sub> with egg albumin.<sup>45</sup> The cloudy solution of gold salt containing egg albumin changes into a golden brown solution when irradiated with microwave (Fig. S1a†). The protein acts as both a catalyst and stabilizer in the reaction. The microwave treatment time was optimized to achieve the maximum emission. The solution began emitting red emission after 3 minutes of microwave treatment, with an intensity increase up to 10 minutes of microwave treatment time, after which the emission intensity reached saturation (Fig. S1b†). The morphology of the synthesized Au NCs was observed using TEM (Fig. 1a and b). The obtained Au NCs were spherical in shape with an average diameter of 4.27 ± 1.27 nm (Fig. 1a, inset) which is in accordance with the reported literature.<sup>46</sup>

The MXene sheets were synthesized using the chemical etching method and delaminated using TMAOH (TMA<sup>+</sup>-Ti<sub>3</sub>C<sub>2</sub>). The delaminated sheets were further treated with alkali media at 80 °C to induce crumpling. The obtained solution was black in color, well dispersed and did not show any visible aggregation in the aqueous phase. This may be attributed to the good delamination property of TMAOH in





**Scheme 1** Synthesis procedure of the folic acid conjugated MXene gold composite (FA\_Au@c-Ti<sub>3</sub>C<sub>2</sub>).

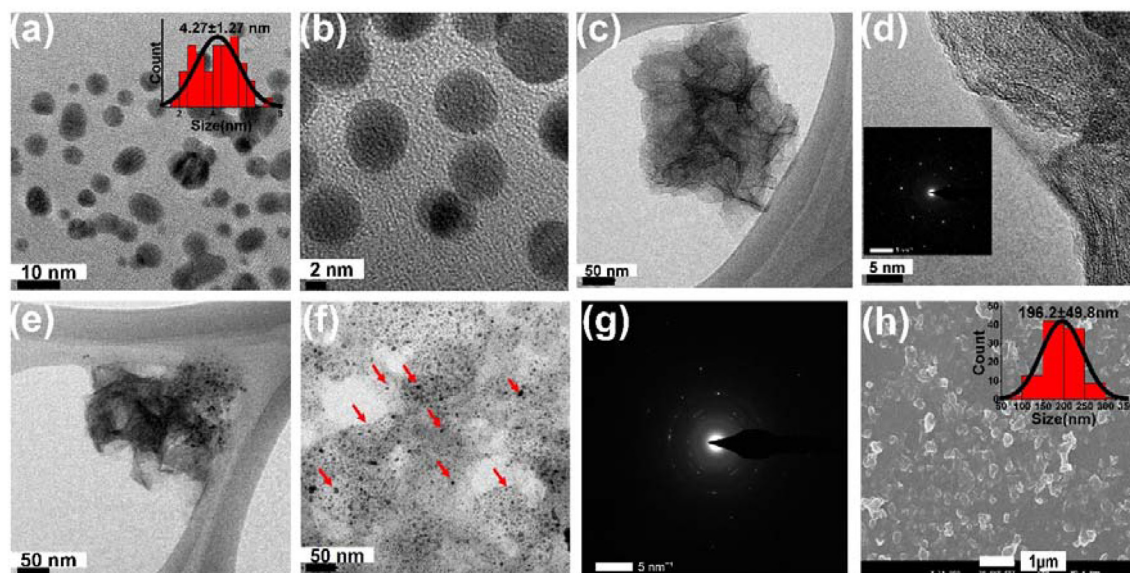


**Fig. 1** Morphological characterization: (a) TEM image (inset: size distribution) of gold nanoclusters [scale: 10 nm]. (b) HRTEM of gold nanoclusters [scale: 2 nm]. (c) TEM image of crumpled MXene sheets (c-Ti<sub>3</sub>C<sub>2</sub>) [scale: 50 nm]. (d) HRTEM of c-Ti<sub>3</sub>C<sub>2</sub> [scale: 5 nm] (inset: diffraction pattern). (e and f) TEM image [scale: 50 nm] and (g) SAED pattern of gold nanocluster conjugated crumpled MXene sheets (Au@c-Ti<sub>3</sub>C<sub>2</sub>). (h) SEM image of FA\_Au@c-Ti<sub>3</sub>C<sub>2</sub> [scale: 1 μm] (inset: size distribution).

conjunction with heat treatment in NaOH solution (used to induce wrinkles). Crumpled Ti<sub>3</sub>C<sub>2</sub> sheets (c-Ti<sub>3</sub>C<sub>2</sub>) when observed under TEM showed a wrinkled morphology with multiple folds (Fig. 1c). The crumpling of MXene as observed was due to the self-folding of a thin sheet rather than flocculation of multiple sheets together shown by Di Zhao *et al.*<sup>39</sup> This

alkali induced crumpling gave rise to a 3D-like architecture. The lateral size of the c-Ti<sub>3</sub>C<sub>2</sub> nanosheets was under 400 nm with very thin edges indicating that the nanosheets were mono or few layered (Fig. 1d). The selected area electron diffraction (SAED) pattern showed hexagonal symmetry (Fig. 1d, inset) confirming that c-Ti<sub>3</sub>C<sub>2</sub> is still crystalline in nature. The 3D-

like MXene structure can provide active sites for conjugation of gold nanoclusters.

The surface charge of the nanocomposite was determined using zeta potential which also helped to understand the chemistry behind the conjugation (Fig. S2a†). The surface charge of both  $c\text{-Ti}_3\text{C}_2$  and Au NCs was found to be negative with a magnitude of  $-49.92 \pm 1.1$  (Fig. S2b†) and  $-8.28 \pm 0.67$  mV (Fig. S2c†), respectively. The gold nanocluster conjugation on  $c\text{-Ti}_3\text{C}_2$  was done with the help of triethylamine (TEA) which is a tertiary amine having positive charge. The addition of TEA to  $c\text{-Ti}_3\text{C}_2$  resulted in the change of surface charge from  $-49.92 \pm 1.1$  to  $-21.85 \pm 0.56$  mV (Fig. S2d†). The considerable change in the zeta potential after the addition of TEA indicates the amine functionalization of  $c\text{-Ti}_3\text{C}_2$  through electrostatic absorption. The amine functional groups on  $c\text{-Ti}_3\text{C}_2$  and negatively charged gold nanoclusters were incubated overnight and purified afterwards ( $\text{Au}@c\text{-Ti}_3\text{C}_2$ ). The surface charge of  $\text{Au}@c\text{-Ti}_3\text{C}_2$  was found to be  $-19.87 \pm 0.86$  mV (Fig. S2e†). The gold nanoclusters can be observed to be dispersed evenly on the surface of crumpled MXene sheets under the effect of electrostatic interaction (Fig. 1e and f). This shows that the efficient assembly of the Au NCs on  $c\text{-Ti}_3\text{C}_2$  can be achieved through the use of amine functionalization. The SAED pattern shows the semi crystalline nature of the material compared to the hexagonal arrangement confirming the presence of both gold and MXene together (Fig. 1g). Elemental mapping confirmed the presence of Ti (titanium), Au (gold), O (oxygen), and N (nitrogen) (Fig. S3†). To compare the effect of morphology on loading percentage, gold conjugation was also done on flat  $\text{Ti}_3\text{C}_2$  nanosheets ( $\text{TMA}^+\text{-Ti}_3\text{C}_2$ ). The TEM images showed very few gold nanoclusters on flat sheets (Fig. S4†). The gold content was evaluated through ICP and it was observed that compared to  $\text{TMA}^+\text{-Ti}_3\text{C}_2$ , the crumpled sheets ( $c\text{-Ti}_3\text{C}_2$ ) showed a 2.14-fold increase in the conjugated gold concentration. The 3D like structure with wrinkles and ridges may act as a pocket to hold an increased amount of gold nanoclusters compared to flat plain sheets. The same kind of phenomenon could be observed by Xing He *et al.* while loading vancomycin on crumpled graphene oxides compared to flat graphene oxides.<sup>47</sup> This work shows a novel strategy not only to obtain crumpled MXene sheets, but also to load higher gold content.

In order for nanoparticles (NPs) to be effective in biomedicine, they must meet certain criteria. These include outperforming conventional agents in *in vitro* or *in vivo* applications while causing minimal cytotoxicity. NPs must also be able to efficiently reach their intended destination by avoiding non-specific interactions with plasma proteins and evade the reticuloendothelial system. Additionally, NPs must maintain their colloidal stability under physiological conditions and preferably over a wide pH range. NPs must also localize to the targeted location to avoid unwanted interaction with normal healthy cells. As a result, chemical modification of the NP surface is often necessary to allow specific interactions with target cells.<sup>48</sup> In this work,  $\text{Au}@c\text{-Ti}_3\text{C}_2$  was further conjugated with folic acid ( $\text{FA\_Au}@c\text{-Ti}_3\text{C}_2$ ) to develop and enhance

specific targeting of cancer cells while limiting the side effects. Folic acid is one of the most widely used compounds that could target the folate receptors on tumor cells. The obtained solution was greenish black in color. The size distribution of  $\text{FA\_Au}@c\text{-Ti}_3\text{C}_2$  as observed with SEM (Fig. 1h) was found to show a small lateral size of  $196.23 \pm 49.85$  nm (Fig. 1h, inset) which might be beneficial for biomedical application. The surface charge of  $\text{FA\_Au}@c\text{-Ti}_3\text{C}_2$  was determined to be  $-29.95 \pm 1.5$  mV (Fig. S2f†) indicating good stability of the material.

### 3.2 Structural and chemical characterization

AFM was employed to measure the thickness of the nanosheets formed (Fig. 2a–c). The thickness of Au NCs (Fig. 2a) and  $c\text{-Ti}_3\text{C}_2$  (Fig. 2b) was found to be  $2.44 \pm 0.38$  nm and  $2.22 \pm 0.49$  nm, respectively. The lateral thickness of  $c\text{-Ti}_3\text{C}_2$  shows the presence of single-to-double-layer MXene or single layer folded one. The thickness of  $\text{Au}@c\text{-Ti}_3\text{C}_2$  (Fig. 2c) increased to  $4.7 \pm 0.26$  nm representing the successful conjugation of AuNCs on the surface of  $c\text{-Ti}_3\text{C}_2$ . Fig. 2d shows the comparison of the thicknesses of Au NCs,  $c\text{-Ti}_3\text{C}_2$  and  $\text{Au}@c\text{-Ti}_3\text{C}_2$ .

XRD was used to understand the structural characteristics of the nanomaterial synthesized (Fig. 2e). The characteristic peaks of the (001) and (002) planes are observed at  $9.49^\circ$  and  $19.04^\circ$  in the MAX phase ( $\text{Ti}_3\text{AlC}_2$ ).<sup>49</sup> The peaks of the planes shift to lower angles after etching with hydrofluoric acid which leads to successful removal of aluminium atoms from the MAX phase. The peak of the (001) plane at  $9.49^\circ$  in the MAX phase shifts to  $8.96^\circ$  and  $8.03^\circ$  in  $\text{HF-Ti}_3\text{C}_2$  and  $\text{TMA}^+\text{-Ti}_3\text{C}_2$ , respectively, suggesting a significant increase in interlayer spacing. As an effect of Al etching, the interlayer spacing change can be recognized through the shift in this peak.<sup>50</sup> The disappearance of the peak at  $38.65^\circ$  of the (104) plane indicates  $\text{Ti}_3\text{AlC}_2$  exhaustion and proves that the generated MXene is a pure phase.<sup>51</sup> The crumpled MXene ( $c\text{-Ti}_3\text{C}_2$ ) showed (001) and (002) peaks at  $7.09^\circ$  and  $14.21^\circ$ , respectively, indicating further delamination leading to one or two layered thick MXene sheets. The observation of a strong peak in the XRD pattern of Au NCs was difficult due to other elements present in egg protein. Smaller  $2\theta$  peaks were observed for Au NCs at  $45.5^\circ$  corresponding to the (111) lattice plane.<sup>52</sup> The peaks for the (001) and (002) planes could be observed at  $6.58^\circ$  and  $14.51^\circ$  in  $\text{Au}@c\text{-Ti}_3\text{C}_2$  along with other characteristic peaks of MXene. However, in  $\text{Au}@c\text{-Ti}_3\text{C}_2$ , peaks at  $27.15^\circ$  and  $31.86^\circ$  were also observed due to the formation of  $\text{Ti}_3\text{C}_2(\text{OH})_2$ .<sup>53,54</sup> The result indicates that the nanocomposite contains surface hydroxyl groups which may be attributed to the deposition of gold nanoclusters on the MXene sheets. The surface modification and conjugation of  $\text{Au}@c\text{-Ti}_3\text{C}_2$  with folic acid did not lead to any phase change in  $\text{FA\_Au}@c\text{-Ti}_3\text{C}_2$ .

XPS and FTIR analyses were performed to understand the chemical conjugation of the material at different synthesis steps. Gold salt reacts with egg albumin to generate Au NCs. The Au NCs further conjugated with  $c\text{-Ti}_3\text{C}_2$  and folic acid can thus have a range of functional groups on their surface, resulting in diverse bonding environments. For  $\text{FA\_Au}@c\text{-Ti}_3\text{C}_2$ , Ti

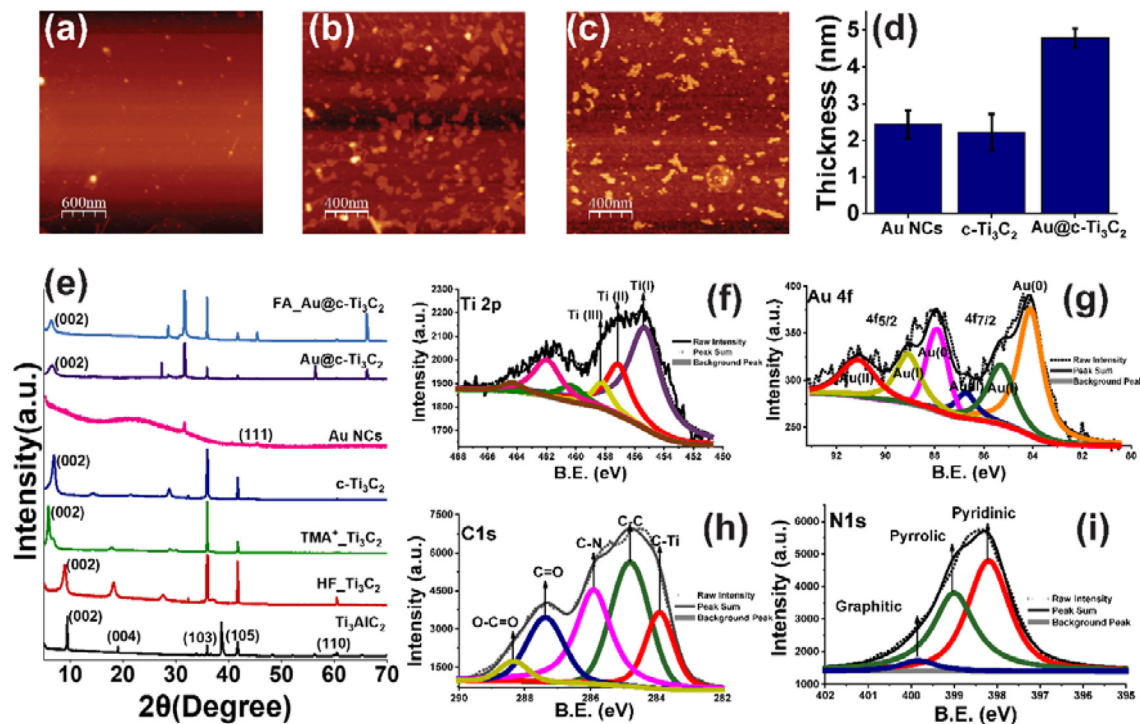


Fig. 2 AFM images of (a) Au NCs, (b) c-Ti<sub>3</sub>C<sub>2</sub>, and (c) Au@c-Ti<sub>3</sub>C<sub>2</sub>; (d) graph showing the thickness of Au NCs, c-Ti<sub>3</sub>C<sub>2</sub>, and Au@c-Ti<sub>3</sub>C<sub>2</sub>; (e) XRD spectra. High resolution deconvoluted XPS scans for (f) Ti 2p, (g) Au 4f, (h) C 1s, and (i) N 1s spectra of FA\_Au@c-Ti<sub>3</sub>C<sub>2</sub>.

2p spectra show the presence of Ti<sup>1+</sup> (455.3/460.3 eV), Ti<sup>2+</sup> (457.1/461.9 eV) and Ti<sup>3+</sup> (458.2/464.3 eV) assigned to 2p<sub>3/2</sub> and 2p<sub>1/2</sub>, respectively (Fig. 2f). The three peaks may arise from the Ti-C attached to different surface termination groups and are commonly attributed to Ti-C-TiO<sub>2</sub>, Ti-C-TiF<sub>3</sub>, and Ti-C-TiF<sub>2</sub>. XPS showed minimal surface oxide functional groups which are found in the Ti 2p regions in the form of TiO<sub>2</sub> peaks. The maximum peaks at 84.1 and 87.9 eV in the Au 4f deconvoluted spectra correspond to 4f<sub>7/2</sub> and 4f<sub>5/2</sub>, respectively (Fig. 2g). In contrast to the peak locations of bulk Au (84.0 and 87.4 eV), this positive shift occurs when the cluster size is decreased. Au 4f<sub>7/2</sub> and 4f<sub>5/2</sub> could further be deconvoluted into Au(0), Au(I) and Au(III). The peaks for Au(0), Au(I), and Au(III) were centered at 84.09, 85.34, and 86.75 eV for Au 4f<sub>7/2</sub>, and at 87.93, 89.09, and 91.14 eV for Au 4f<sub>5/2</sub>.<sup>55,56</sup> The C 1s spectrum (Fig. 2h) includes C-Ti at 283.8 eV, C-C at 284.8 eV, C-N at 285.9 eV, C=O at 287.4 eV and O-C=O at 288.3 eV. The N 1s spectra (Fig. 2i) show pyridinic (398.1 eV), pyrrolic (399.07 eV) and graphitic (399.8 eV) peaks. The presence of nitrogen in the material can be mostly due to the conjugation of folic acid, which is a nitrogen rich compound.

FTIR analyses (Fig. S5†) show that the HF assisted etching of the MAX phase leads to a peak around 1024 cm<sup>-1</sup> in c-Ti<sub>3</sub>C<sub>2</sub> which can be linked to the F-terminated carbon. A peak appearing at 1650 cm<sup>-1</sup> is attributed to C=O stretching. The peak at 1542 cm<sup>-1</sup> representing the symmetric vibrations of the carboxylic group in c-Ti<sub>3</sub>C<sub>2</sub> is overlapped by the broad peak of the NH group of the folic acid at 1550–1700 cm<sup>-1</sup>. A peak at 2923 cm<sup>-1</sup> which might be due to the C-H stretching appears

to be more prominent in Au NCs. Another broad peak observed at 3456 cm<sup>-1</sup> can be attributed to O-H stretching and is accentuated in FA\_Au@c-Ti<sub>3</sub>C<sub>2</sub> because of the carboxylic acid bonds present in FA. The presence of the -OH bond in FA\_Au@c-Ti<sub>3</sub>C<sub>2</sub> signifies that a successful conjugation of FA with Au@c-Ti<sub>3</sub>C<sub>2</sub> may have taken place. Furthermore, the reduction in the C-H peak in FA\_Au@c-Ti<sub>3</sub>C<sub>2</sub> in comparison with that of AuNCs may be due to the bonding of C-H groups with c-Ti<sub>3</sub>C<sub>2</sub>. The FTIR spectrum clearly shows that folic acid has been effectively coupled to Au@c-Ti<sub>3</sub>C<sub>2</sub>.

### 3.3 Optical characterization

The UV-vis-NIR absorption spectra for various steps in the formation of the nanoconjugate are shown in Fig. 3a. The TMAOH delaminated MXene sheets (TMA<sup>+</sup>-Ti<sub>3</sub>C<sub>2</sub>) show a maximum absorbance peak at 278 nm and a broad absorbance in the NIR region. In crumpled MXene (c-Ti<sub>3</sub>C<sub>2</sub>), the maximum absorbance peak shifts to 263 nm with a similar broad absorbance in the NIR region. The gold nanoclusters, however, show a peak at 229 nm only, with no absorbance in the NIR region. The conjugation of gold nanoclusters with crumpled MXene (Au@c-Ti<sub>3</sub>C<sub>2</sub>) gave rise to broad absorbance in the UV-visible range from 300 to 600 nm and also a broad peak in the NIR region of 750–1100 nm. This indicates the successful conjugation of gold nanoclusters with c-Ti<sub>3</sub>C<sub>2</sub> exhibiting a synergistic absorbance. The folic acid conjugation gives rise to a sharp peak at 265 nm with an increase in the intensity in the visible and NIR region. The absorbance in the visible and NIR region paves the way for FA\_Au@c-Ti<sub>3</sub>C<sub>2</sub> to be applied as a





**Fig. 3** (a) Absorbance spectra; (b) fluorescence images of egg albumin, Au NCs, Au@c-Ti<sub>3</sub>C<sub>2</sub>, and FA\_Au@c-Ti<sub>3</sub>C<sub>2</sub> under UV light. Fluorescence spectra of Au NCs and Au@c-Ti<sub>3</sub>C<sub>2</sub> at excitation wavelengths of (c) 250 nm and (d) 300 nm; (e) contact angle of FA\_Au@c-Ti<sub>3</sub>C<sub>2</sub> (500  $\mu\text{g mL}^{-1}$ ); (f) digital image of FA\_Au@c-Ti<sub>3</sub>C<sub>2</sub> dispersed in Milli-Q, PBS and complete DMEM; (g) digital image of FA\_Au@c-Ti<sub>3</sub>C<sub>2</sub> dispersed in water (1), methanol (2), ethanol (3), isopropyl alcohol (4), acetic acid (5), ethyl acetate (6), dimethylformamide (7), dimethylsulfoxide (8), acetone (9), acetonitrile (10), and dichloromethane (11).

bimodal theranostic tool for bio-imaging and as a photothermal agent.<sup>57,58</sup> The nanomaterial dispersions were irradiated under UV light to observe their fluorescence (Fig. 3b). Gold nanoclusters showed deep red emission when observed under UV-light while egg albumin did not display any emission. Au@c-Ti<sub>3</sub>C<sub>2</sub> showed light red while FA\_Au@c-Ti<sub>3</sub>C<sub>2</sub> showed pinkish red fluorescence when observed under UV-light.

The fluorescence property of the synthesized material was confirmed with the help of photoluminescence spectroscopy (Fig. 3c and d). Gold nanoclusters showed  $\lambda_{\text{max}}$  emission at 356 nm when excited with 250 nm, which red shifted to 395 nm in Au@c-Ti<sub>3</sub>C<sub>2</sub> which is due to the conjugation of gold nanoclusters with c-Ti<sub>3</sub>C<sub>2</sub>. When the excitation wavelength was increased to 300 nm the gold nanoclusters showed a maximum emission wavelength of 363 nm while Au@c-Ti<sub>3</sub>C<sub>2</sub> showed a very broad emission in the range of 300–500 nm. These results demonstrate that both materials exhibit excitation-dependent fluorescence.

### 3.4 Wettability and colloidal stability

Contact angle is used to measure the wettability of a dispersion. The shape that a drop will take on a surface is determined by the surface tension of the fluid and the properties of

the surface. Contact angle is used to qualitatively ascertain whether a material is hydrophilic ( $<90^\circ$ ) or hydrophobic ( $>90^\circ$ ). Properties including surface roughness, surface energy, surface chemistry, and surface coatings influence the wettability of a material. The contact angle of FA\_Au@c-Ti<sub>3</sub>C<sub>2</sub> was determined to be  $39.25 \pm 2.5^\circ$ , showing a primarily hydrophilic character (Fig. 3e).

The colloidal stability of FA\_Au@c-Ti<sub>3</sub>C<sub>2</sub> was evaluated in several solvents. Stable dispersion in both aqueous and complete media is an integral property of any material with potential for use in bio-applications. FA\_Au@c-Ti<sub>3</sub>C<sub>2</sub> exhibited excellent dispersion in Milli-Q water, PBS, and Dulbecco's modified Eagle's medium supplemented with fetal bovine serum (c-DMEM) (Fig. 3f). The material stability in the aforesaid solvents was tested for up to 5 days (Fig. S6†), as c-DMEM turned yellow on the fifth day owing to a common shift in its pH. Up to this point, the material showed excellent stability. The dispersion of the material was also further investigated in a few protic and aprotic solvents. Fig. 3g shows the digital images of FA\_Au@c-Ti<sub>3</sub>C<sub>2</sub> dispersed in various solvents such as water, methanol, ethanol, isopropyl alcohol, acetic acid, ethyl acetate, dimethylformamide, dimethylsulfoxide, acetone, acetonitrile, and dichloromethane. The material dispersed well in all the

solvents except in dichloromethane in which it showed precipitation.

### 3.5 Toxicity assessment of FA\_Au@c-Ti<sub>3</sub>C<sub>2</sub>

**3.5.1 *In vitro* study.** The toxicity of a nanomaterial governs its potential application in biological systems. Nanoparticles after entering the body may pass through physiological barriers, interact with cells, evade immune recognition, and circulate in the blood stream. They may interfere with cellular function or promote harmful cellular responses. It has been observed that the toxicity of nanoparticles differs in different cell models and, therefore, it is crucial to examine the toxicity in various cellular models to ensure the non-toxic nature of a material. Here, the cytotoxicity of FA\_Au@c-Ti<sub>3</sub>C<sub>2</sub> was examined in cultured mammalian cell models such as mouse fibroblast L929, MDA-MB-231 breast cancer cell line, and THP-1 differentiated macrophages. Hemolysis analysis was performed to check the toxic effect of the material on human red blood cells. Resazurin sodium salt was used as an indicator for *in vitro* cell viability assay. FA\_Au@c-Ti<sub>3</sub>C<sub>2</sub> did not exhibit any toxicity in L929 up to 250  $\mu\text{g mL}^{-1}$  and showed more than 80% cellular viability (Fig. 4a). The viability decreased to <75% at a concentration of 500  $\mu\text{g mL}^{-1}$ . The breast cancer model MDA-MB-231 cell line was also utilized to check the toxicity of FA\_Au@c-Ti<sub>3</sub>C<sub>2</sub>. The cellular viability was more than 80% up to a concentration of 250  $\mu\text{g mL}^{-1}$  following which the cellular

viability decreased drastically. Cellular proliferation analyses were performed using propidium iodide dye which is a membrane-impermeable fluorescent DNA stain (Fig. 4b). The dye binds to DNA by intercalating between bases and enables measurement of cellular DNA content in various stages such as the G1 phase, S phase, and G2 phase of the cell cycle. Flow cytometry analysis confirmed that L929 cells treated with 100 and 250  $\mu\text{g mL}^{-1}$  FA\_Au@c-Ti<sub>3</sub>C<sub>2</sub> [Fig. 4b(ii and iii)] for 24 hours did not show any changes in the distribution of cell cycle phases when compared with untreated cells [Fig. 4b(i)]. The effect of FA\_Au@c-Ti<sub>3</sub>C<sub>2</sub> on the morphology of L929 was also observed under E-SEM. The magnified images of L929 cells cultured with NPs show a spindle cell morphology with a single, clearly visible nucleus, cell-to-cell contacts and filopodia extension similar to that in control cells. There was no change in the morphology of L929 cells incubated with various concentrations (25, 150 and 250  $\mu\text{g mL}^{-1}$ ) of FA\_Au@c-Ti<sub>3</sub>C<sub>2</sub> compared to control cells (Fig. 4c) which indicates that the material does not cause any adverse effect on the cultured cells.<sup>59</sup> These studies suggest that FA\_Au@c-Ti<sub>3</sub>C<sub>2</sub> does not have any negative effect on the growth of monolayer cultured cells up to 250  $\mu\text{g mL}^{-1}$ . The immunotoxicity of nanomaterials was explored using THP-1 differentiated macrophages (Fig. 4d). FA\_Au@c-Ti<sub>3</sub>C<sub>2</sub> shows >75% cell viability up to 120  $\mu\text{g mL}^{-1}$  after a 24-hour exposure. There were no evident changes in the morphology of macrophages post treatment.

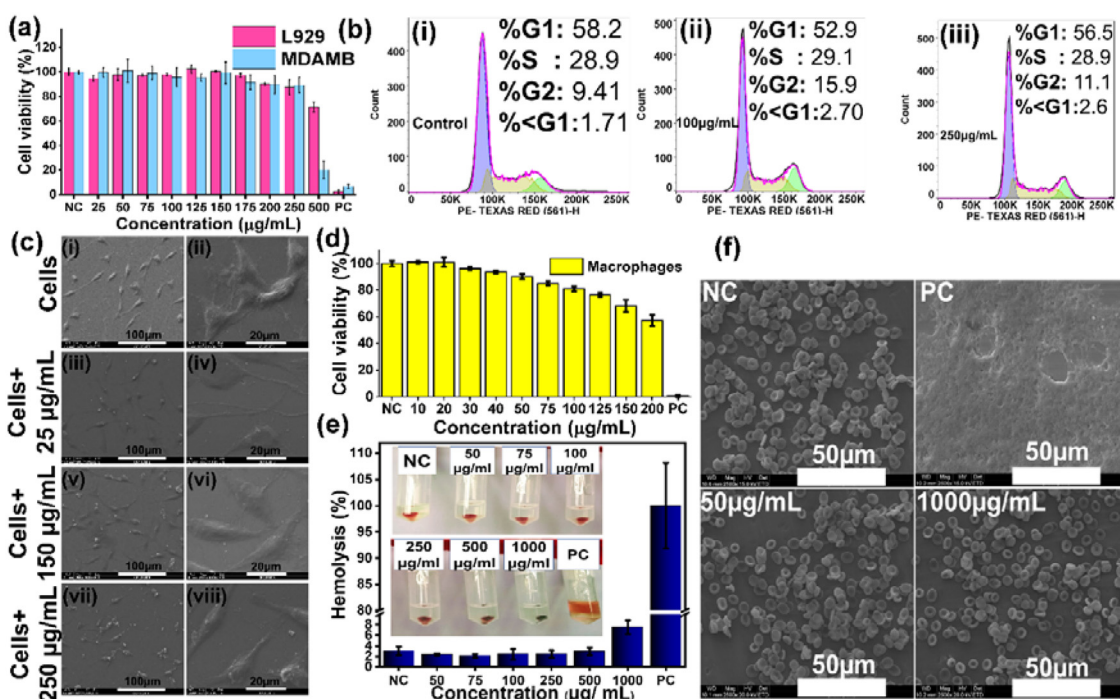


**Fig. 4** Toxicity study of FA\_Au@c-Ti<sub>3</sub>C<sub>2</sub>. (a) L929 and MDAMB cell lines incubated with concentrations in the range of 25–500  $\mu\text{g mL}^{-1}$ ; (b) cell cycle analysis using propidium iodide dye in (i) untreated L929 cells (control), (ii) L929 cells incubated with 100  $\mu\text{g mL}^{-1}$ , and (iii) L929 cells incubated with 250  $\mu\text{g mL}^{-1}$ ; (c) SEM images of L929 cells: (i and ii) control cells, (iii and iv) treated with 25  $\mu\text{g mL}^{-1}$ , (v and vi) treated with 150  $\mu\text{g mL}^{-1}$  and (vii and viii) treated with 250  $\mu\text{g mL}^{-1}$ ; (d) macrophages incubated with concentrations of 10–200  $\mu\text{g mL}^{-1}$ ; (e) hemocompatibility study by incubation with concentrations of 50–1000  $\mu\text{g mL}^{-1}$  (inset – digital images of the supernatant of RBCs incubated with 50–1000  $\mu\text{g mL}^{-1}$ ); (f) E-SEM images of RBCs showing RBCs treated with PBS (NC), Triton-X (PC), and 50  $\mu\text{g mL}^{-1}$  and 1000  $\mu\text{g mL}^{-1}$  FA\_Au@c-Ti<sub>3</sub>C<sub>2</sub>.



The cell viability reduced to 70% at  $150 \mu\text{g mL}^{-1}$  followed by 58% at  $200 \mu\text{g mL}^{-1}$ .

Hemocompatibility testing is another significant evaluation in nano-therapeutics as nanomaterials come into contact with blood immediately if injected intravenously. Hemocompatibility is mostly dependent on concentration, structure, size and shape of nanomaterials.<sup>60</sup> The adverse effect of nanomaterials in blood includes hemolysis which was tested using human red blood cells in this study (Fig. 4e). Here, Triton-X-100 was taken as a positive control as it is known to cause disruption of the RBCs, while PBS was considered as a negative control as it has no hemolytic activity. The Triton-X treated cells gave a red supernatant upon centrifugation confirming the disruption of RBCs and the presence of hemoglobin in the solution. The PBS and nanomaterial-treated cells showed a good pellet and a clear supernatant indicating intact RBCs. The quantitative hemolytic activity was checked by measuring the absorbance of the supernatant. FA\_Au@c-Ti<sub>3</sub>C<sub>2</sub> showed <5% hemolysis up to  $500 \mu\text{g mL}^{-1}$  similar to PBS demonstrating the high hemocompatibility of the synthesized nanomaterial. The morphology of the treated RBCs was visualised under E-SEM for the qualitative assay (Fig. 4f) as the cell-NP interactions can cause significant erythrocyte aggregation, detrimental morphological changes and cytoskeletal distortions. PBS-treated RBCs

showed an oval biconcave disk-shaped morphology. There also was no change in the morphology and the number density of the RBCs post exposure to FA\_Au@c-Ti<sub>3</sub>C<sub>2</sub>. No morphology could be observed in Triton-X treated red blood cells due to the disruption. All the above cytotoxic studies indicate the non-toxicity of FA\_Au@c-Ti<sub>3</sub>C<sub>2</sub> in a wide range of tested concentrations and also suggest that the biocompatibility of the nanomaterial varies according to the cell line probably due to the difference in the metabolism, morphology and permeability.<sup>61</sup>

**3.5.2 *In vivo* toxicity study (oral administration).** Male and female rats treated with the FA\_Au@Ti<sub>3</sub>C<sub>2</sub> nanocomposite showed no behavioral abnormalities or body weight difference during the study period (Fig. 5a and b). There were also no significant differences in the organ weight/body weight coefficients of the vital organs in both male (Fig. S7†) and female rats (Fig. S8†) compared to those of the respective control rats. The organ weight/body weight coefficients of the reproductive organs of the male and female rats treated with nanoparticles also did not show any difference compared to those of the control rats. Hematological analysis also showed no significant difference between male and female rats (Fig. 5c).

Fig. 6a presents the analysis of the serum biochemistry. The liver is the key organ engaged in human metabolism and detoxification. SGPT and SGOT are enzymes found in the liver

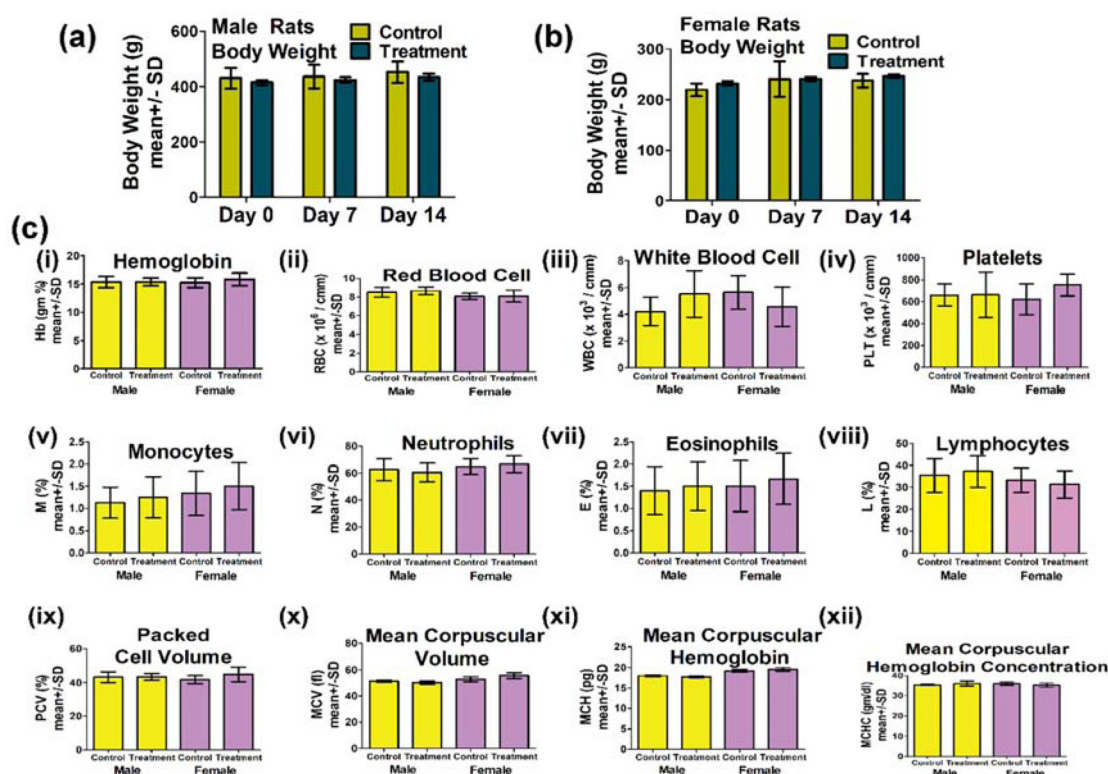


**Fig. 5** *In vivo* acute toxicity of orally administered FA\_Au@c-Ti<sub>3</sub>C<sub>2</sub> at a dose of  $20 \text{ mg kg}^{-1}$ . Comparison of the body weight of control and FA\_Au@c-Ti<sub>3</sub>C<sub>2</sub> treated rats at 0-day, 7th day and 14th day for (a) male rats and (b) female rats; (c) hematology data of male and female Wistar rats: (i) hemoglobin, (ii) red blood cells, (iii) white blood cells, (iv) platelets, (v) monocytes, (vi) neutrophils, (vii) eosinophils, (viii) lymphocytes, (ix) packed cell volume, (x) mean corpuscular volume, (xi) mean corpuscular hemoglobin, and (xii) mean corpuscular hemoglobin concentration.



**Fig. 6** (a) Analysis of the serum biochemistry. The values are expressed as mean  $\pm$  SD ( $n = 6$ ); (b) histopathological observation of the liver, kidneys, lungs, heart and brain of control male, treatment male, control female, and treatment female rats after hematoxylin and eosin staining (scale: 500  $\mu$ m).

and cardiac cells and are released into the bloodstream in the case of liver or heart damage.<sup>62</sup> The normal values of SGPT and SGOT indicate the non-toxic nature of FA\_Au@Ti<sub>3</sub>C<sub>2</sub> towards liver function. Normal levels of bilirubin also indicate normal functioning of the liver in all the treated rats. Comparable triglyceride, cholesterol and high-density lipoprotein concentrations indicate that there is no metabolism imbalance of lipids in mice. The difference in triglyceride levels between male and female rats is due to the fact that compared to similarly aged male rats, female rats are more effective in removing triglycer-

ides from plasma.<sup>63,64</sup> Creatinine is generally used for evaluation of renal damage and acts as a kidney function parameter, and there was no observed significant difference in its level too. Histopathology is one of the most critical evaluation parameters for determining the toxicity of a nano-formulation. The microscopy images of vital organs such as the liver, kidneys, lungs, heart and brain did not show any abnormalities in either male or female treated rats (Fig. 6b).

**3.5.3 *In vivo* toxicity study (I.V. administration).** The same set of experiments were also conducted using the I.V. route of



administration for FA\_Au@Ti<sub>3</sub>C<sub>2</sub> treated male and female Wistar rats. The body/organ weights of male (Fig. S9†) and female rats (Fig. S10†) did not show any difference. Hematology study was also performed. All the hematological parameters showed no abnormality except platelet number (Fig. S11 and S12†). The male and female rats showed an increase in platelets when FA\_Au@Ti<sub>3</sub>C<sub>2</sub> was administered through the I.V. mode. Various metallic particles are known to interact with platelets.<sup>65</sup> The most probable reason for this phenomenon could be the functional groups, surface charge, and surface area; however, the exact cause or mechanism is still unknown.<sup>66–68</sup> The serum biochemistry was also evaluated and it showed no abnormalities (Fig. S13†).

### 3.6 Cellular imaging and uptake

The localization study of FA\_Au@c-Ti<sub>3</sub>C<sub>2</sub> in cells was performed using confocal microscopy (Fig. 7a). The nucleus was

labelled using DAPI. The cells showed the inherent bright red fluorescence of FA\_Au@c-Ti<sub>3</sub>C<sub>2</sub> at a very low concentration of 12 µg mL<sup>-1</sup> in the cytoplasm compared with the localization of DAPI in the nucleus. The intensity of red emission increased as the concentration of the material was increased to 25 µg mL<sup>-1</sup>. These results imply the usefulness of FA\_Au@c-Ti<sub>3</sub>C<sub>2</sub> as a bioimaging agent. The quantitative uptake of NPs was evaluated using ICP-AES (Fig. 7b). FA\_Au@c-Ti<sub>3</sub>C<sub>2</sub> showed an excellent uptake of ~35% in MDAMB cells in the 1st hour of incubation itself. The uptake increased as the incubation time increased. It showed ~70% uptake in 12 hours. This may be attributed to the folic acid conjugation which ensures better cellular uptake of the material.

AFM was used to examine the uptake of the material by cancer cells and study the impact of internalization on the cell surface (Fig. 7c). In the control cells, a very well-defined nucleus, cytoplasmic region and lamellipodium could be

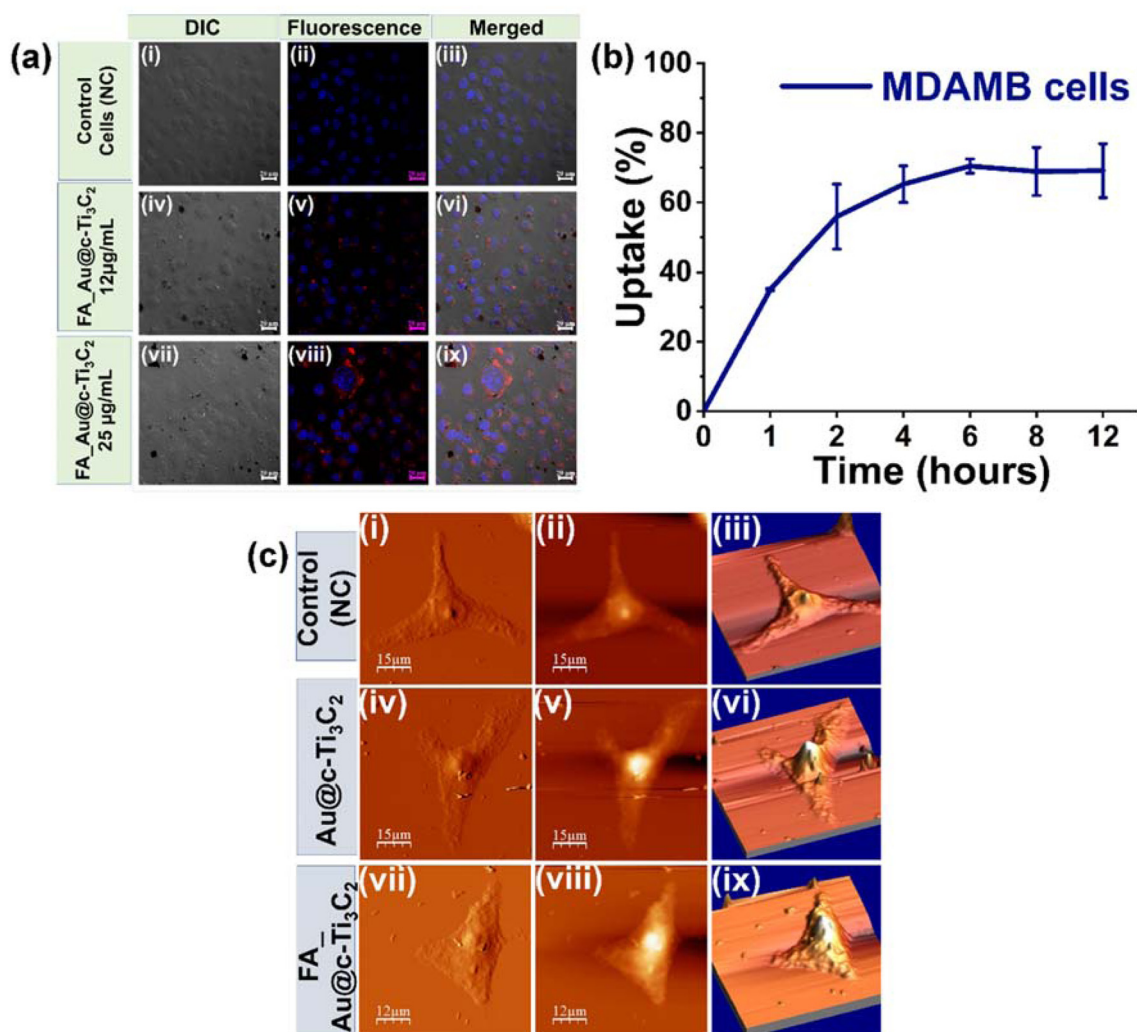


**Fig. 7** (a) Confocal images representing DIC, fluorescence, and merged images of (i–iii) control MDAMB cells, (iv–vi) cells treated with 12 µg mL<sup>-1</sup> FA\_Au@c-Ti<sub>3</sub>C<sub>2</sub> and (vii–ix) cells treated with 25 µg mL<sup>-1</sup> FA\_Au@c-Ti<sub>3</sub>C<sub>2</sub> [scale: 20 µm]. (b) Graph showing the cellular uptake of FA\_Au@c-Ti<sub>3</sub>C<sub>2</sub> up to 12 hours obtained using ICP-AES. (c) AFM images showing the uptake of materials: (i–iii) control MDAMB cells, (iv–vi) cells treated with Au@c-Ti<sub>3</sub>C<sub>2</sub>, and (vii–ix) cells treated with FA\_Au@c-Ti<sub>3</sub>C<sub>2</sub>.



observed. A similar observation could be made in the Au@-Ti<sub>3</sub>C<sub>2</sub> treated cells, but the cytoskeleton of the cells appeared more compact in the 2D view in the case of FA\_Au@-Ti<sub>3</sub>C<sub>2</sub>. No cell membrane disruption was observed in the treated cells. Further, the roughness and height of control cells and treated cells were compared (Fig. S14†). For the height, two regions, that is, the nucleus and cytoskeleton, were selected and compared (Fig. S14a–c†). There was a very slight difference in the height of the nucleus region of control, Au@-Ti<sub>3</sub>C<sub>2</sub> and FA\_Au@-Ti<sub>3</sub>C<sub>2</sub> treated cells (Fig. S14d†). The difference in height was more pronounced in the cytoskeleton region (Fig. S14e†). FA\_Au@-Ti<sub>3</sub>C<sub>2</sub> treated cells showed the minimum height among the samples. The cell surface roughness also increased slightly in the case of Au@-Ti<sub>3</sub>C<sub>2</sub> and FA\_Au@-Ti<sub>3</sub>C<sub>2</sub> compared to control (Fig. S14f†). These analyses suggest that the cell flattening and roughness may be accredited to cellular interaction with nanoparticles and their internalization by endocytosis and show that the folic acid helps in enhanced uptake of the material.<sup>69</sup>

### 3.7 Photothermal transduction and *in vitro* photothermal cytotoxicity

The notable absorbance in the biological NIR window of FA\_Au@-Ti<sub>3</sub>C<sub>2</sub> prompts its application in photothermal therapy. The temperature profile showed a concentration dependent increase in temperature (Fig. 8a). When the material with a concentration of 100 µg mL<sup>-1</sup> (corresponding to 10 ppm of titanium as evaluated by ICP-AES) was irradiated with an 808 nm laser, the temperature increased from 37 °C to 48.3 ± 2.4 °C within 5 minutes and remained stable until

10 minutes. When the concentration was increased to 200 µg mL<sup>-1</sup>, the temperature increased to 56.36 ± 3.7 °C within 5 minutes. No temperature increase was observed in Milli-Q water under similar conditions. Cyclic PTT was examined by heating the same sample repeatedly. FA\_Au@-Ti<sub>3</sub>C<sub>2</sub> showed stability up to 5 cycles (Fig. 8b). The photothermal conversion efficiency of FA\_Au@-Ti<sub>3</sub>C<sub>2</sub> was calculated to be 43.51% (Fig. S15†).

The cytotoxicity of the PTT treatment using FA\_Au@-Ti<sub>3</sub>C<sub>2</sub> was examined in MDAMB cells. The induced cytotoxicity was found to be dependent on both concentration and laser irradiation time. There was around ~70% decrease in cellular viability when incubated with 30 ppm titanium and laser irradiated for 10 min with an 808 nm laser at 2 W. There was complete cancer cell ablation as the concentration was increased to 40 ppm (Fig. 8c). Cytotoxicity was also observed with respect to laser irradiation time where the laser irradiation was performed for 3, 5, 7, and 10 minutes at 40 ppm titanium (Fig. 8d). The cytotoxicity increased as the laser irradiation time increased from 3 to 10 minutes. Cells treated with laser alone or nanoparticles alone (40 ppm) did not show any cell death demonstrating the safety and specificity of the treatment.

### 3.8 Mechanism of induced cell death

Necrosis and apoptosis are two possible ways of cell death produced by PTT. Necrosis is an unfavourable mechanism for cell death since the aberrant release of intracellular contents, including damage-associated molecular patterns (DAMPs), into the extracellular environment might elicit harmful inflam-

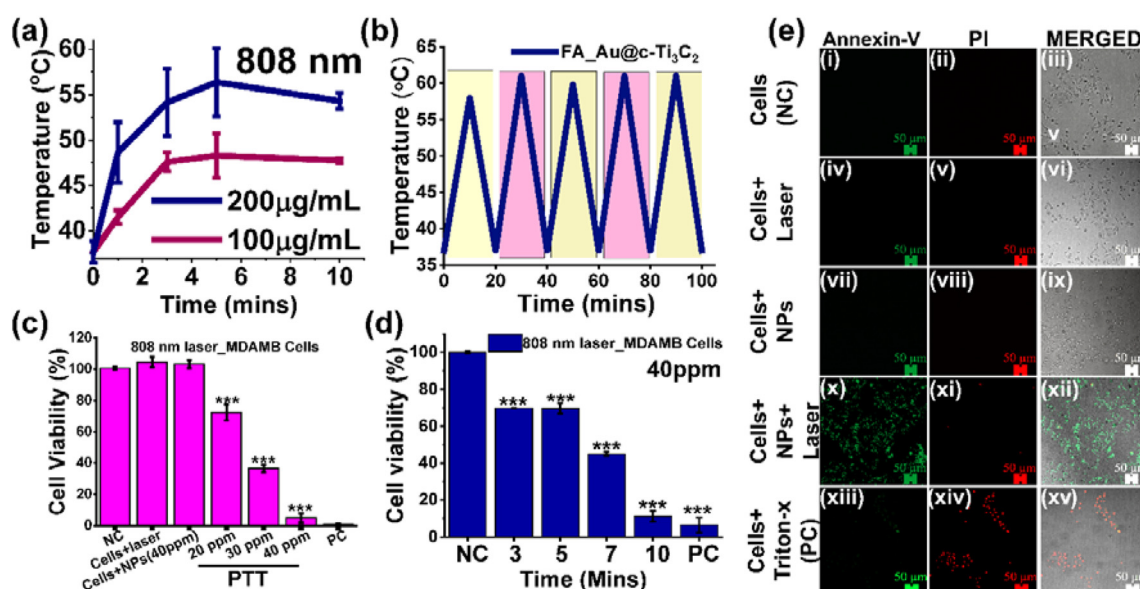


**Fig. 8** (a) Photothermal temperature profile of FA\_Au@-Ti<sub>3</sub>C<sub>2</sub> irradiated with an 808 nm laser up to 10 minutes. (b) Cyclic PTT profile of FA\_Au@-Ti<sub>3</sub>C<sub>2</sub>. (c) Cellular viability of MDAMB cells treated with FA\_Au@-Ti<sub>3</sub>C<sub>2</sub> and irradiated with an 808 nm laser at different concentrations. (d) Cellular viability of MDAMB cells treated with FA\_Au@-Ti<sub>3</sub>C<sub>2</sub> and irradiated with an 808 nm laser for 3, 5, 7 and 10 minutes. (e) Fluorescence images of the apoptosis assay performed using Annexin-V PI staining: (i–iii) control cells (NC), (iv–vi) cells + laser, (vii–ix) cells + FA\_Au@-Ti<sub>3</sub>C<sub>2</sub>, (x–xii) cells + FA\_Au@-Ti<sub>3</sub>C<sub>2</sub> + laser and (xiii–xv) cells + Triton-X (PC). Scale: 50 µm.

matory and immunogenic responses.<sup>70</sup> On the other hand, apoptosis, which is also known as programmed cell death, does not cause inflammation and therefore is preferred. Annexin V apoptosis assay (Fig. 8e) was used to detect apoptosis in cells induced by photothermal therapy using FA\_Au@c-Ti<sub>3</sub>C<sub>2</sub>. Annexin V-PI staining can be used to distinguish between viable, apoptotic, and necrotic cells depending upon the cell membrane integrity.<sup>71</sup> Annexin V can bind to anionic phosphatidylserine (PS) exposed to the outer leaflet only when the cell membrane integrity is compromised. Annexin V is co-incubated with propidium iodide (PI) to distinguish viable (both -ve), early apoptotic (Annexin V +ve only), late apoptotic (both +ve) and necrotic cells (PI +ve only). Here, untreated MDAMB cells were considered as negative control while Triton-X 100 incubated cells were considered as positive control. When observed under spinning-disk confocal

microscopy, MDAMB cells (negative control) [Fig. 8e(i-iii)], cells treated with 808 nm laser irradiation alone [Fig. 8e(iv-vi)] and cells treated with NPs alone [Fig. 8e(vii-ix)] did not show any green or red fluorescence indicating the viability of the cells and confirming that no significant reduction in the cell membrane integrity took place. Cells treated with NPs along with laser irradiation (PTT treatment) showed green fluorescence depicting early apoptosis [Fig. 8e(x-xii)]. Cells treated with Triton-X showed very light intensity of green but high red fluorescence depicting late apoptosis [Fig. 8e(xiii-xv)]. The study showed that apoptosis is the primary mechanism of cell death induced by photothermal therapy using FA\_Au@c-Ti<sub>3</sub>C<sub>2</sub>.

The effect of PTT treatment using FA\_Au@c-Ti<sub>3</sub>C<sub>2</sub> on the cell growth was also examined through cell cycle analysis using PI dye (Fig. 9). A propidium iodide DNA profile reveals cells in G1, S, and G2 phases. DNA fragmentation occurs when

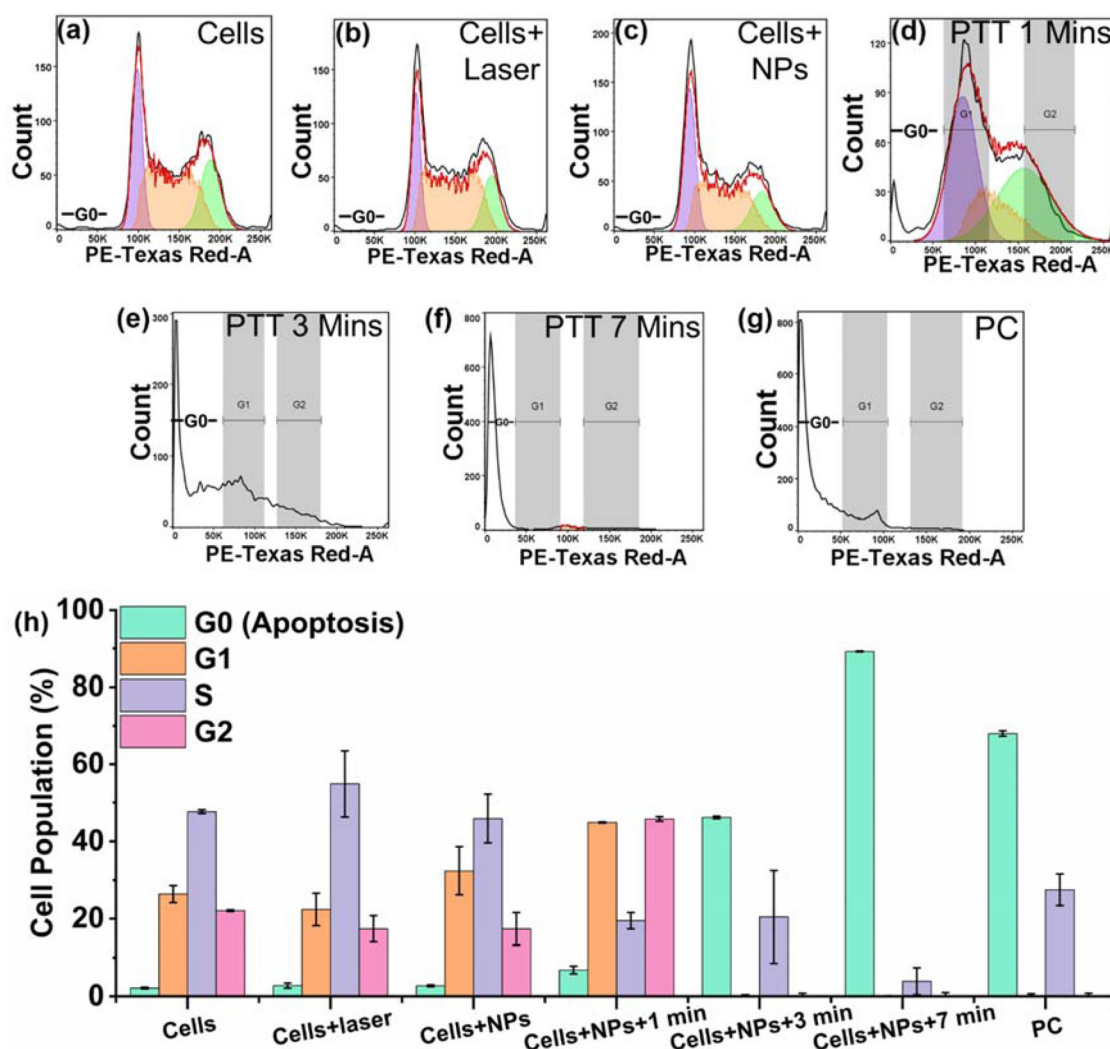


**Fig. 9** FA\_Au@c-Ti<sub>3</sub>C<sub>2</sub> mediated PTT effect on the distribution of the cell cycle in MDA-MB-231 cells. (a) Untreated cells, (b) cells + 808 nm laser, (c) cells + NPs, (d) cells + NPs + 1 min PTT, (e) cells + NPs + 3 min PTT, (f) cells + NPs + 7 min PTT and (g) cells + Triton-X. (h) % of each phase of the cell cycle in the respective group.

cells die and undergo apoptosis. In cell cycle histograms, this may be observed as a population to the left of the G1 peak, indicated by a G0 population.<sup>72</sup> The percentages of the G0, G1, S, and G2 stages of the cell cycle at various laser irradiation times for PTT are depicted in Fig. 9h. Compared to the control group, cells treated with nanoparticles alone or laser irradiation alone did not show any cell damage, as evidenced by the lack of change in the percentage of cell cycle stages. However, changes in the cell cycle of cancer cells were observed following laser treatment with internalized FA\_Au@c-Ti<sub>3</sub>C<sub>2</sub>. Flow cytometry indicated that PTT treatment inhibited cell growth. The widespread distribution of FA\_Au@c-Ti<sub>3</sub>C<sub>2</sub> inside the cytoplasm of irradiated cancer cells may have a major effect post PTT due to the increased temperature. The intracellular temperature increase has a substantial influence on the DNA of cells, resulting in a drop in cell viability. The PTT treatment even after 1 minute of laser irradiation showed an increase in G0 and G1 phases and a decrease in the S phase. These results suggested the occurrence of G1 phase arrest after PTT. As the laser irradiation time increased to 3 and 7 min, respectively, the apoptotic cell number increased and, therefore, the peak can only be observed in the G0 phase. Cells treated with Triton-X 100 were considered as positive control as it causes fragmentation of DNA and cell death when exposed to higher concentration. The PC also showed the peak at G0.

In addition to generating hyperthermia-induced cell death, PTT may have other anticancer effects such as accelerating the generation of reactive oxygen species and improving its own efficacy by triggering photodynamic treatment. ROS, or reactive oxygen species, represent oxygen containing free radical species. It is believed that oxidative damage to DNA, proteins, and lipids caused by ROS stress promotes programmed cell death.<sup>73,74</sup> The hydroxyl radical, superoxide anion, and hydrogen peroxide (H<sub>2</sub>O<sub>2</sub>) are some of the most prevalent reactive oxygen species. 2',7'-Dichlorodihydrofluorescein diacetate (H<sub>2</sub>DCFDA) is the most used probe for detecting cellular H<sub>2</sub>O<sub>2</sub>. In the presence of reactive oxygen intermediates, non-fluorescent H<sub>2</sub>DCFDA is converted to the highly fluorescent 2',7'-dichlorofluorescein (DCF).

Herein also H<sub>2</sub>DCFDA dye was used to evaluate the influence of PTT on ROS formation utilizing FA\_Au@c-Ti<sub>3</sub>C<sub>2</sub> (Fig. S16†). The lack of green fluorescence in the untreated cells (negative control), cells + NIR, and cells + NPs indicates the absence of ROS formation. The cells treated with H<sub>2</sub>O<sub>2</sub> served as the positive control (PC) and exhibited a high level of green fluorescence. The PTT treated cells displayed intense green fluorescence comparable to PC. The intensity of the fluorescence increased as the duration of the laser irradiation extended from 1 to 10 minutes.

All *in vitro* studies indicated that FA\_Au@c-Ti<sub>3</sub>C<sub>2</sub> mediated PTT successfully triggered the death of cancer cells. Annexin V-PI studies and the cell cycle assay indicated that apoptosis was the primary cause of cell death and that PTT-induced apoptosis leads to G1 phase cell cycle arrest. According to the findings of the ROS study, laser therapy can lead to the pro-

duction of reactive oxygen species (photodynamic therapy), which may contribute to the increased cancer cell mortality rate.<sup>75</sup>

## 4. Conclusions, outlook and future aspects

The aim of the work was to design and develop a multifunctional nanocomposite combining MXene sheets and gold nanoclusters. The gold nanoclusters were synthesized from egg albumin using a microwave process and they emitted red fluorescence. MXene sheets, which were crumpled rather than flat, served as both a photothermal agent and a platform for attaching the gold nanoclusters. The resultant crumpled sheets were highly disperse and smaller in size than those previously reported in the published literature, proving to be highly beneficial for cellular internalization and other biomedical applications. The crumpled shape of the MXene sheets also showed better loading of the gold nanoclusters than flat sheets. When functionalized with folic acid, the resulting nanoconstruct (FA\_Au@c-Ti<sub>3</sub>C<sub>2</sub>) exhibited red fluorescence derived from the Au NCs and a photothermal effect due to the MXene sheets.

Herein, the toxicity of FA\_Au@c-Ti<sub>3</sub>C<sub>2</sub> was investigated using Wistar male and female rats at a dosage of 20 mg kg<sup>-1</sup> after 14 days of intravenous and oral administration, respectively. The weight/organ coefficient, hematological analysis, blood serum biochemistry, and histopathology were utilized to assess the influence of the nanocomposite delivery route on rats. When delivered orally, FA\_Au@c-Ti<sub>3</sub>C<sub>2</sub> showed no harmful effects which also opens a pathway for future application of MXene based nanomaterials in gastro-intestinal applications. However, there was a little increase in platelet count with intravenous delivery. Aside from that, no negative effects were found. The detailed toxicity investigation indicates that better functionalization or passivation might be performed to minimize any adverse reactions in the I.V. mode and make the material more bio-compatible.

The photothermal transduction study of FA\_Au@c-Ti<sub>3</sub>C<sub>2</sub> was done using an 808 nm laser and it exhibited a photothermal conversion efficiency of 43.51%. It showed a photothermal response of 48.3 °C in 5 minutes at a concentration of 100 µg mL<sup>-1</sup>, which increased to 56.3 °C when the concentration was increased to 200 µg mL<sup>-1</sup>. FA\_Au@c-Ti<sub>3</sub>C<sub>2</sub> demonstrated no cytotoxicity up to 250 µg mL<sup>-1</sup> in L929 mouse fibroblast cells. Its fluorescence and photothermal effects on breast cancer cells were used to image and eradicate cancer cells *in vitro*. The mechanism of *in vitro* cell death through photothermal therapy (PTT) was determined to be apoptosis. Overall, FA\_Au@c-Ti<sub>3</sub>C<sub>2</sub> shows outstanding photothermal activity and no *in vivo* toxicity whether administered orally or intravenously. All of the investigations indicated that the material might be employed as an image guided PTT agent in the future.



## Author contributions

Conceptualization – R. S., B. S.; data curation – B. S., R. B., P. M.; methodology – B. S., R. S., D. S.; investigation – B. S., R. B., P. M.; formal analysis – B. S., R. B., P. M., D. S., R. S.; supervision – R. S., M. G., D. S.; writing – original draft – B. S., R. B.; writing – review & editing – P. M., D. S., M. G., R. S.

## Conflicts of interest

The authors declare no conflicts of interest.

## Acknowledgements

The authors acknowledge the Sophisticated Analytical Instrumentation Facility (SAIF), India, and the Industrial Research Consultancy Centre (IRCC), Indian Institute of Technology Bombay (IITB), for providing central instrumentation facility. The authors acknowledge the National Institute for Research in Reproductive and Child Health, Mumbai, Maharashtra, for carrying out *in vivo* toxicity studies in rats. B. S. acknowledges the Department of Biotechnology, India. We also acknowledge Dr Sourabh Mehta (PhD, IITB) for technical discussions.

## References

- P. Kiran, A. Khan, S. Neekhara, P. Kumar, B. Singh, S. Pallod, F. Dias and R. Srivastava, *BioSensing, Theranostics, and Medical Devices*, Springer, Singapore, 2022, pp. 59–82.
- X. Li, G. Fan and C. Zeng, *Int. J. Hydrogen Energy*, 2014, **39**, 14927–14934.
- B. Singh, R. Bahadur, M. Gandhi and R. Srivastava, *Polym. Bull.*, 2022, **11**, 521–534.
- A. A. Aljabali, B. Al-Trad, L. Al Gazo, G. Alomari, M. Al Zoubi, W. Alshaer, K. Al-Batayneh, B. Kanan, K. Pal and M. M. Tambuwala, *J. Mol. Struct.*, 2021, **1231**, 130009.
- A. I. El-Batal, F. M. Mosallam, M. M. Ghorab, A. Hanora, M. Gobara, A. Baraka, M. A. Elsayed, K. Pal, R. M. Fathy, M. Abd Elkodous and G. S. El-Sayyad, *Int. J. Biol. Macromol.*, 2020, **156**, 1584–1599.
- A. I. El-Batal, F. M. Mosallam, M. M. Ghorab, A. Hanora, M. Gobara, A. Baraka, M. A. Elsayed, K. Pal, R. M. Fathy, M. Abd Elkodous and G. S. El-Sayyad, *Int. J. Biol. Macromol.*, 2020, **156**, 1584–1599.
- S. Asiya, K. Pal, S. Kralj, G. S. El-Sayyad, F. G. de Souza and T. Narayanan, *Mater. Today Chem.*, 2020, **17**, 100327.
- G. Eskiizmir, A. T. Ermertcan and K. Yapici, *Nanostructures for Oral Medicine*, Elsevier, 2017, pp. 511–544.
- X. Qu, Y. Li, L. Li, Y. Wang, J. Liang and J. Liang, *J. Nanomater.*, 2015, **2015**, DOI: [10.1155/2015/784097](https://doi.org/10.1155/2015/784097).
- M. M. Xu, T. T. Jia, B. Li, W. Ma, X. Chen, X. Zhao and S. Q. Zang, *Chem. Commun.*, 2020, **56**, 8766–8769.
- Y. Li, T. Zhai, J. Chen, J. Shi, L. Wang, J. Shen and X. Liu, *Chem. – Eur. J.*, 2022, **28**, e202103736.
- M. Tang, J. Zhang, C. Yang, Y. Zheng and H. Jiang, *Front. Chem.*, 2020, **8**, 1–17.
- N. Kaur, R. N. Aditya, A. Singh and T. R. Kuo, *Nanoscale Res. Lett.*, 2018, **13**, 1–12.
- Y. Xu, P. Zhang, Z. Wang, S. Lv and C. Ding, *Microchim. Acta*, 2018, **185**, 1–7.
- D. Li, Q. Liu, Q. Qi, H. Shi, E. C. Hsu, W. Chen, W. Yuan, Y. Wu, S. Lin, Y. Zeng, Z. Xiao, L. Xu, Y. Zhang, T. Stoyanova, W. Jia and Z. Cheng, *Small*, 2020, **16**(43), DOI: [10.1002/sml.202003851](https://doi.org/10.1002/sml.202003851).
- K. Pal, N. Asthana, A. A. Aljabali, S. K. Bhardwaj, S. Kralj, A. Penkova, S. Thomas, T. Zaheer and F. Gomes de Souza, *Crit. Rev. Solid State Mater. Sci.*, 2022, **47**, 691–707.
- L. Shang and G. U. Nienhaus, *Biophys. Rev.*, 2012, **4**, 313–322.
- S. M. van de Looij, E. R. Hebel, M. Viola, M. Hembury, S. Oliveira and T. Vermonden, *Bioconjugate Chem.*, 2022, **33**, 4–23.
- Y. Yang, S. Wang, C. Wang, C. Tian, Y. Shen and M. Zhu, *Chem. – Asian J.*, 2019, **14**, 1418–1423.
- H. Cui, Z. S. Shao, Z. Song, Y. B. Wang and H. S. Wang, *J. Mater. Chem. C*, 2020, **8**, 14312–14333.
- J. F. Y. Fong, Y. H. Ng and S. M. Ng, *Fullerenes, Graphenes and Nanotubes: A Pharmaceutical Approach*, William Andrew Publishing, 2018, pp. 227–295.
- K. Pal, N. Asthana, A. A. Aljabali, S. K. Bhardwaj, S. Kralj, A. Penkova, S. Thomas, T. Zaheer and F. Gomes de Souza, *Crit. Rev. Solid State Mater. Sci.*, 2022, **47**, 691–707.
- K. Pal, A. Si, G. S. El-Sayyad, M. A. Elkodous, R. Kumar, A. I. El-Batal, S. Kralj and S. Thomas, *Crit. Rev. Solid State Mater. Sci.*, 2021, **46**, 385–449.
- M. Alhabeb, K. Maleski, T. S. Mathis, A. Sarycheva, C. B. Hatter, S. Uzun, A. Levitt and Y. Gogotsi, *Angew. Chem., Int. Ed.*, 2018, **57**, 5444–5448.
- G. Deysher, C. E. Shuck, K. Hantanasirisakul, N. C. Frey, A. C. Foucher, K. Maleski, A. Sarycheva, V. B. Shenoy, E. A. Stach, B. Anasori and Y. Gogotsi, *ACS Nano*, 2020, **14**, 204–217.
- B. Singh, R. Bahadur, S. Neekhara, M. Gandhi and R. Srivastava, *ACS Appl. Mater. Interfaces*, 2021, **13**, 3011–3023.
- H. Liu, Z. Wang, J. Wang, Y. Yang, S. Wu, C. You, N. Tian and Y. Li, *Nanoscale*, 2022, **14**, 9218–9247.
- W. Xi, J. Jin, Y. Zhang, R. Wang, Y. Gong, B. He and H. Wang, *Nanoscale*, 2022, **14**, 11923–11944.
- A. Sengupta, B. V. B. Rao, N. Sharma, S. Parmar, V. Chavan, S. K. Singh, S. Kale and S. Ogale, *Nanoscale*, 2020, **12**, 8466–8476.
- H. Rastin, B. Zhang, A. Mazinani, K. Hassan, J. Bi, T. T. Tung and D. Losic, *Nanoscale*, 2020, **12**, 16069–16080.
- S. Kyrylenko, O. Gogotsi, I. Baginskiy, V. Balitskiy, V. Zahorodna, Y. Husak, I. Yanko, M. Pernakov, A. Roshchupkin, M. Lyndin, B. B. Singer, V. Buranych, A. Pogrebnyak, O. Sulaieva, O. Solodovnyk, Y. Gogotsi and

- M. Pogorielov, *ACS Appl. Mater. Interfaces*, 2022, **14**, 28683–28696.
- 32 D. Cui, N. Kong, L. Ding, Y. Guo, W. Yang and F. Yan, *Adv. Healthcare Mater.*, 2021, **10**, 2101215.
- 33 S. Pan, J. Yin, L. Yu, C. Zhang, Y. Zhu, Y. Gao and Y. Chen, *Adv. Sci.*, 2020, **7**, 1901511.
- 34 J. B. Lee, G. H. Choi and P. J. Yoo, *J. Alloys Compd.*, 2021, **887**, 161304.
- 35 Z. Yang, L. Jiang, J. Wang, F. Liu, J. He, A. Liu, S. Lv, R. You, X. Yan, P. Sun, C. Wang, Y. Duan and G. Lu, *Sens. Actuators, B*, 2021, **326**, 128828.
- 36 X. Zhang, J. Miao, P. Zhang, Q. Zhu, M. Jiang and B. Xu, *Chin. Chem. Lett.*, 2020, **31**, 2305–2308.
- 37 S. A. Shah, T. Habib, H. Gao, P. Gao, W. Sun, M. J. Green and M. Radovic, *Chem. Commun.*, 2017, **53**, 400–403.
- 38 M. C. Fokker, S. Janbaz and A. A. Zadpoor, *RSC Adv.*, 2019, **2019**, 5174–5188.
- 39 D. Zhao, M. Clites, G. Ying, S. Kota, J. Wang, V. Natu, X. Wang, E. Pomerantseva, M. Cao and M. W. Barsoum, *Chem. Commun.*, 2018, **54**, 4533–4536.
- 40 G. P. Lim, C. F. Soon, N. L. Ma, M. Morsin, N. Nayan, M. K. Ahmad and K. S. Tee, *Environ. Res.*, 2021, **201**, 111592.
- 41 K. Zheng, S. Li, L. Jing, P. Y. Chen and J. Xie, *Adv. Healthcare Mater.*, 2020, **9**, 2001007.
- 42 W. Tang, Z. Dong, R. Zhang, X. Yi, K. Yang, M. Jin, C. Yuan, Z. Xiao, Z. Liu and L. Cheng, *ACS Nano*, 2019, **13**, 284–294.
- 43 R. Rajamanikandan and M. Ilanchelian, *ACS Omega*, 2018, **3**, 14111–14118.
- 44 H. Li, M. Yang, D. Kong, R. Jin, X. Zhao, F. Liu, X. Yan, Y. Lin and G. Lu, *Sens. Actuators, B*, 2019, **282**, 366–372.
- 45 J. Tian, L. Yan, A. Sang, H. Yuan, B. Zheng and D. Xiao, *J. Chem. Educ.*, 2014, **91**, 1715–1719.
- 46 J. Tian, L. Yan, A. Sang, H. Yuan, B. Zheng and D. Xiao, *J. Chem. Educ.*, 2014, **91**, 1715–1719.
- 47 X. He, Z. Zhou, Z. Han, Y. Zeng, X. Chen and J. Su, *ACS Omega*, 2019, **4**, 12252–12258.
- 48 N. T. K. Thanh and L. A. W. Green, *Nano Today*, 2010, **5**, 213–230.
- 49 A. Tariq, S. I. Ali, D. Akinwande and S. Rizwan, *ACS Omega*, 2018, **3**, 13828–13836.
- 50 B. Singh, R. Bahadur, M. Gandhi and R. Srivastava, *Polym. Bull.*, 2022, **1**–14.
- 51 W. Feng, H. Luo, Y. Wang, S. Zeng, L. Deng, X. Zhou, H. Zhang and S. Peng, *RSC Adv.*, 2018, **8**, 2398–2403.
- 52 S. Govindaraju, S. R. Ankireddy, B. Viswanath, J. Kim and K. Yun, *Sci. Rep.*, 2017, **7**, 1–12.
- 53 X. Li, G. Fan and C. Zeng, *Int. J. Hydrogen Energy*, 2014, **39**, 14927–14934.
- 54 A. Iqbal and N. M. Hamdan, *Materials*, 2021, **14**(21), 6292.
- 55 K. Selvaprakash and Y. C. Chen, *Biosens. Bioelectron.*, 2014, **61**, 88–94.
- 56 X. Yang, Q. Pan, Y. Ao, J. Du, Z. Dong, M. Zhai and L. Zhao, *Environ. Sci. Pollut. Res.*, 2020, **27**, 38334–38343.
- 57 R. Li, L. Zhang, L. Shi and P. Wang, *ACS Nano*, 2017, **11**, 3752–3759.
- 58 X. Wang, M. Yao, L. Ma, P. Yu, T. Lu, L. Zhang, X. Yuan, Y. Zhang and J. Ye, *Adv. Healthcare Mater.*, 2021, **10**, 2100392.
- 59 B. Singh, R. Bahadur, M. Rangara, M. N. Gandhi and R. Srivastava, *ACS Appl. Bio Mater.*, 2021, **4**, 4641–4651.
- 60 K. M. De La Harpe, P. P. D. Kondiah, Y. E. Choonara, T. Marimuthu, L. C. Du Toit and V. Pillay, *Cells*, 2019, **8**(10), 1209.
- 61 A. Szuplewska, D. Kulpińska, A. Dybko, A. M. Jastrzębska, T. Wojciechowski, A. Rozmysłowska, M. Chudy, I. Grabowska-Jadach, W. Ziemkowska, Z. Brzózka and A. Olszyna, *Mater. Sci. Eng., C*, 2019, **98**, 874–886.
- 62 R. Hassankhani, M. Esmaeillou, A. A. Tehrani, K. Nasirzadeh, F. Khadir and H. Maadi, *Environ. Sci. Pollut. Res.*, 2015, **22**, 1127–1132.
- 63 G. M. Reaven, *J. Gerontol.*, 1978, **33**, 368–371.
- 64 G. C. Shearer, J. A. Joles, H. Jones, R. L. Walzem and G. A. Kaysen, *Kidney Int.*, 2000, **57**, 2268–2274.
- 65 N. K. Hante, C. Medina and M. J. Santos-Martinez, *Front. Cardiovasc. Med.*, 2019, **6**, 139.
- 66 S. J. Montague, P. Patel, E. M. Martin, A. Slater, L. G. Quintanilla, G. Perrella, C. Kardeby, M. Nagy, D. Mezzano, P. M. Mendes and S. P. Watson, *Platelets*, 2021, **32**, 1018–1030.
- 67 A. N. Ilinskaya and M. A. Dobrovolskaia, *Nanomedicine*, 2013, **8**, 969–981.
- 68 E. Fröhlich, *Curr. Med. Chem.*, 2016, **23**, 408.
- 69 C. Hoskins, A. Cuschieri and L. Wang, *J. Nanobiotechnol.*, 2012, **10**, 1–11.
- 70 J. R. Melamed, R. S. Edelstein and E. S. Day, *ACS Nano*, 2015, **9**, 6–11.
- 71 M. B. Rivas Aiello, J. C. Azcárate, E. Zelaya, P. David Gara, G. N. Bosio, T. Gensch and D. O. Mártire, *Biomater. Sci.*, 2021, **9**, 2608–2619.
- 72 H. Murad, M. Hawat, A. Ekhtiar, A. Aljapawe, A. Abbas, H. Darwish, O. Sbenati and A. Ghannam, *Cancer Cell Int.*, 2016, **16**, 1–11.
- 73 X. Hou, Y. Tao, Y. Pang, X. Li, G. Jiang and Y. Liu, *Int. J. Cancer*, 2018, **143**, 3050–3060.
- 74 S. K. Debnath, B. Singh, N. Agrawal and R. Srivastava, *Handbook of Oxidative Stress in Cancer: Therapeutic Aspects*, Springer, Singapore, 2022, pp. 1–28.
- 75 B. Singh, C. Patnaik, R. Bahadur, M. Gandhi, A. De and R. Srivastava, *Nanoscale*, 2023, DOI: [10.1039/D2NR05283K](https://doi.org/10.1039/D2NR05283K).